

Supporting Information

Layered NiO/Reduced Graphene Oxide Composites by Heterogeneous Assembly with Enhanced Performance as High- performance asymmetric supercapacitor Cathode

Qian Li^{a,b,#}, Qiang Wei^{c,#}, Lijing Xie^{*d}, Chengmeng Chen^{*d}, Chunxiang Lu^{*a}, Fang-Yuan Su^d and
Pucha Zhou^a

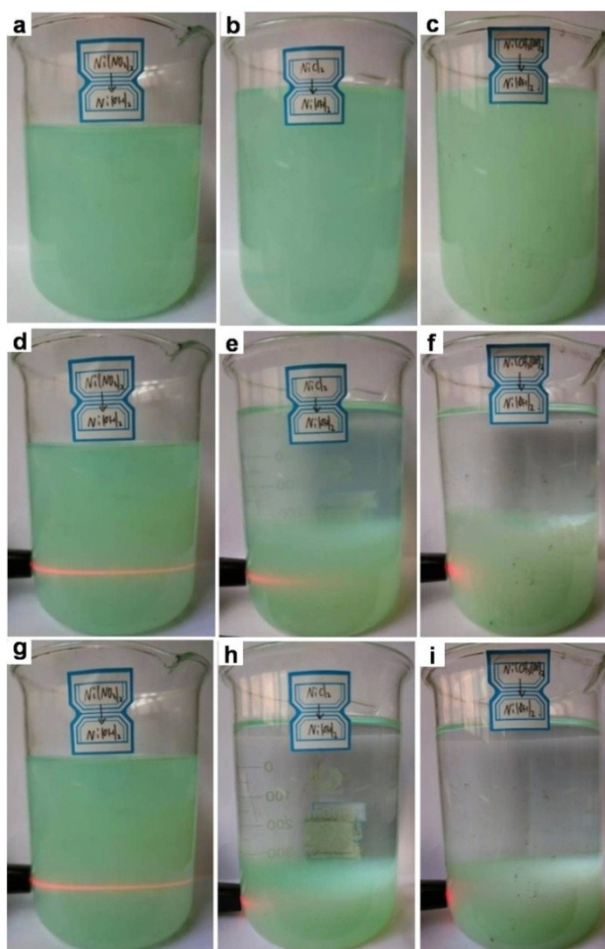


Figure S1. Digital images of the exfoliated Ni(OH)₂ nanosheets suspension with different setting time and relevant Tyndall effect. The NO₃⁻-intercalated Ni(OH)₂ nanosheets suspension with (a)12, (d)36, (g)72 hours setting time. The Cl⁻-intercalated Ni(OH)₂ nanosheets suspension with (b)12, (e)36, (h)72 hours setting time. The CH₃COO⁻-intercalated Ni(OH)₂ nanosheets suspension with (c)12, (f)36, (i)72 hours setting time.

Table S1 Zeta potentials of the three Ni(OH)₂ nanosheets suspensions with different anions

different anions	NO ₃ ⁻	Cl ⁻	CH ₃ COO ⁻
Zeta Potential of Ni(OH) ₂ nanosheets (mV)	31.8	20.6	18.2

The effect of different anions on the exfoliation and stability of Ni(OH)₂ nanosheets were investigated. As can be seen in the Figure S1, the NO₃⁻-intercalated Ni(OH)₂ nanosheets suspension is very stable as setting time prolongs. Clear Tyndall light scattering can be discerned even at 72 hours setting time, showing the presence of exfoliated Ni(OH)₂ nanosheets in water. However, the Cl⁻-intercalated and CH₃COO⁻-intercalated Ni(OH)₂ nanosheets suspensions show the obvious settling phenomena, and Tyndall effect gradually disappears as setting time prolongs. The zeta potentials of the three Ni(OH)₂ nanosheets suspensions (Table 1) also indicated that NO₃⁻ ion is more favorable for the exfoliation and stability of Ni(OH)₂ nanosheets.

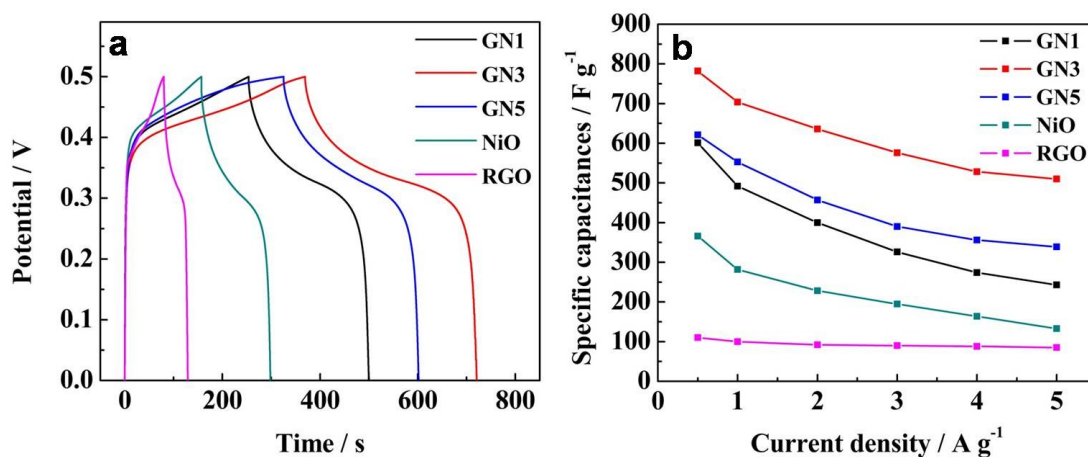


Figure S2. (a) Discharge curves of NiO, RGO and NiO/RGO composites electrode with different mass ratio of NiO to RGO at the current density of 1 A g⁻¹, (b) Specific capacitances of NiO, RGO and NiO/RGO composites electrodes with different mass ratio of NiO to RGO at different current densities.

Figure S2(a) shows the discharge curves of pure NiO, RGO and NiO/RGO composites electrode with different mass ratio of NiO to RGO at the current density of 1 A g⁻¹. The specific capacitance of GN3 was calculated to be 704 F g⁻¹, which is

significantly higher than that of RGO (98 F g^{-1}), NiO (282 F g^{-1}), GN1 (492 F g^{-1}) and GN5 (553 F g^{-1}). As can be seen in Figure S2(b), the specific capacitances of the NiO/RGO composites electrode with different mass ratio of NiO to RGO are much larger than that of pure NiO and RGO at different current densities. Especially, the GN3 exhibits the maximum specific capacitance among the three NiO/RGO composites, indicating that the synergistic effect of NiO and RGO brings out the best in the nanocomposite.

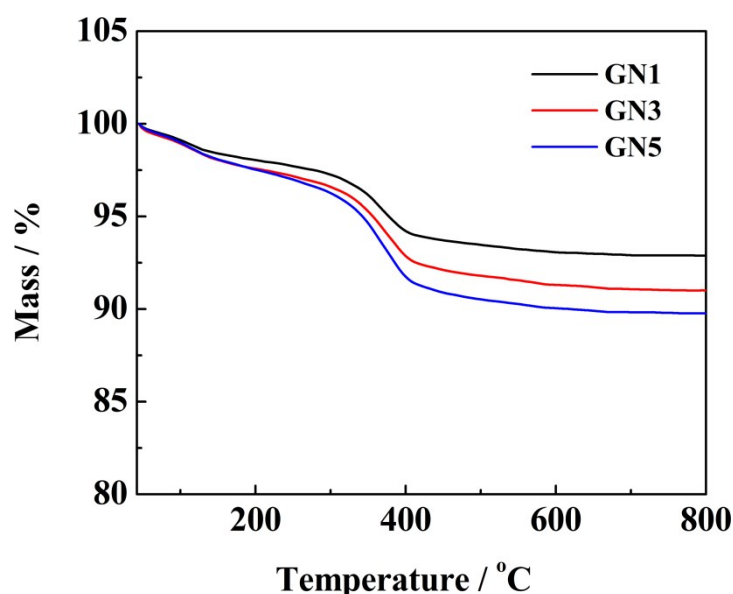


Figure S3. TGA curves of GN1, GN3, GN5.

As shown in Figure S3, with the temperature increased from room temperature to $150 \text{ }^\circ\text{C}$, the NiO/RGO composites exhibit a small mass loss, which is attributed to the removal of adsorbed water. And the main mass loss between $300 \text{ }^\circ\text{C}$ and $400 \text{ }^\circ\text{C}$ is due to the thermal decomposition of RGO.¹ After $600 \text{ }^\circ\text{C}$, the TGA curves tend to be stable without any further obvious weight loss, indicating the decomposition of RGO is completed. The residual weight ratio is the content of NiO in the NiO/RGO composite. Therefore, the mass ration of NiO:RGO in GN1, GN3 and GN5 based on TGA curves are about 92.9:7.1, 91.0:9.0 and 89.8:10.2, respectively.

Table S2 The calculated specific capacitance, power density and energy density of the GN3//AC asymmetrical supercapacitor at different current densities

Current density (A g ⁻¹)	Discharge time (s)	Specific capacitance (F g ⁻¹)	Power density (W kg ⁻¹)	Energy density (Wh kg ⁻¹)
0.5	312	104	375	32.50
1	152	101.3	750	31.66
2	69	92	1500	28.75
3	42.5	85	2250	26.56
4	30.5	81.3	3000	25.41
5	23	76.7	3750	23.97
8	12.5	66.7	6000	20.84
10	9.5	63.3	7500	19.78

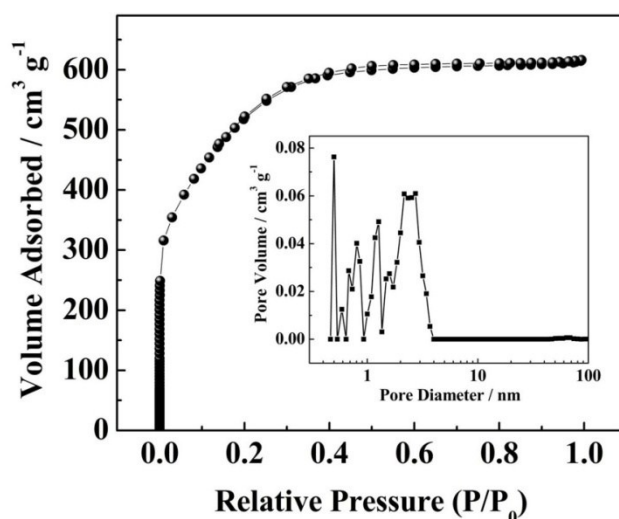


Figure S4. (a) Nitrogen adsorption-desorption isotherms of AC. The inset shows the corresponding pore size distribution.

The pore structure of AC is obtained from N₂ adsorption-desorption isotherm measurements and pore diameter distributions (Figure S4). The AC exhibits combined characteristics of type I isotherm for low relative pressure (P/P_0) and type IV isotherm for high relative pressure (P/P_0). The steep rise of the isotherm at low relative pressure suggests the presence of micropores, and the hysteresis loop at high relative pressures (0.3-1.0) indicates the existence of mesopores. The pore size distribution is shown in the inset of Figure S4. It can be seen that the micropores peaked at 0.5, 0.8, 1.3 nm and the mesopores peaked at 2.7 nm are dominated. Moreover, the AC shows a Brunauer-Emmett-Teller (BET) surface area of 1893 m² g⁻¹ and a total pore volume of

$0.95 \text{ cm}^3 \text{ g}^{-1}$. All the results above suggest the AC is an attractive materials for supercapacitor applications.

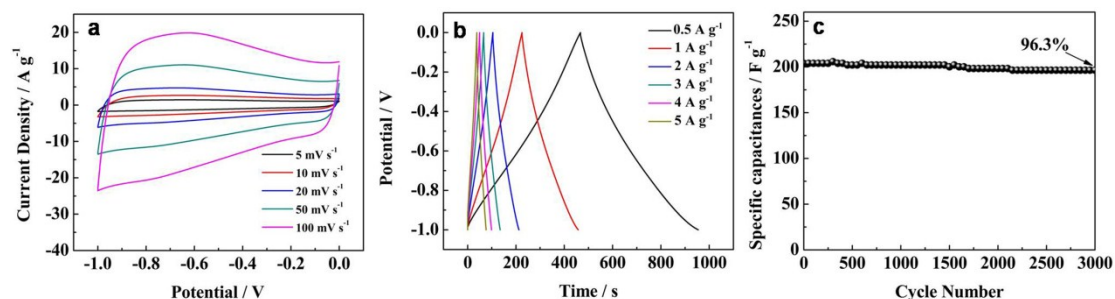


Figure S5. (a) CV curves of AC at different scan rates, (b) Galvanostatic charge-discharge curves of AC at different current densities, (c) Cycling performance of AC at 3 A g^{-1} for 3000 cycles.

The CV curves of AC at different scan rates from 5 to 100 mV s^{-1} are shown in Figure S5(a). As the scan rate increase, the quasi- rectangular shapes of CV curves are well-retained, implying the typical electrical double-layer capacitance. Figure S5(b) shows the galvanostatic charge-discharge curves of AC at different current densities from 0.5 A g^{-1} to 5 A g^{-1} . All these curves are symmetrical and linear, again indicating good electrochemical reversibility and double layer capacitive behavior of AC. Furthermore, the capacitance remains 96.3% of its initial value after 3000 cycles at 3 A g^{-1} , proving the excellent electrochemical stability of AC.

References

- [1] Z. Ji, J. Wu, X. Shen, H. Zhou and H. Xi, *Journal of Materials Science*, 2010, **46**, 1190-1195.